DIRECT SIMULATION OF SOUND GENERATED BY VISCOUS FLOW OVER A CYLINDER USING A TVD METHOD

AXEL ROHDE[*], VLADIMIR V. GOLUBEV[†] AND CLAIRE LESSIAU[‡]
Department of Aerospace Engineering
Embry-Riddle Aeronautical University
Daytona Beach, Florida 32114

ABSTRACT

In the presented work, a new numerical approach to computational aeroacoustic (CAA) problems based on a modified total variation diminishing (TVD) scheme is examined in order to investigate its value as a possible alternative to the more computationally expensive schemes currently used in CAA. Such schemes generally rely on high-order dispersion-relation-preserving (DRP) algorithms. The method is applied to the direct numerical analysis of an unsteady, compressible, viscous 2-D flow over a cylinder at a Mach number of 0.5 and a diameter-based Reynolds number of 100,000. The acoustic signal is extracted directly from the unsteady flowfield solution at several radii and compared to the acoustic predictions based on the Potential-Theoretical Method.

INTRODUCTION

The current study applies a recently developed computational aeroacoustics (CAA) code based on a modified total-variation-diminishing (TVD)[1-10] scheme, to directly compute the sound produced by a 2-D circular cylinder in a viscous flow. This problem was originally included as a category 4 benchmark at the 2nd CAA Workshop[11] where it was specified for incompressible flow of Mach number $M = 0.2$ and transitional Reynolds number $Re = 90,000$ based on the cylinder's diameter D. Such flow parameters presented a significant challenge to the direct numerical simulation of sound at the specified distance of $r/D = 35$ from the cylinder. In fact, none of the contributors in Ref. 11 were able to compute the flow and the acoustic field simultaneously. Instead, most of the participants chose to use RANS or LES to compute the wake-induced unsteady forces on the cylinder, followed by a separate prediction of the Aeolian tones using a surface-integral technique. In the present work, a direct numerical prediction of the unsteady flow and sound is obtained using a numerical algorithm based on the finite-volume description of the unsteady, compressible Navier-Stokes equations. The numerical scheme is formally second-order accurate in space and first-order accurate in time. The inviscid subset of the equations is modeled according to the TVD principle with the numerical viscosity parameter set to zero. This feature preserves the natural formation of the viscous boundary layer and wake flows at Mach numbers $M > 0.3$, but at the same time it makes the current formulation inadequate for incompressible flow predictions. This issue will be addressed in the future. The current version of the code has been applied to simulate a 2-D flow over a cylinder at a Mach number $M = 0.5$ and a diameter-based Reynolds number $Re = 100,000$. No turbulence modeling is implemented for this test case, since the flow is below the transitional Reynolds number of 300,000. The simulation is carried out in a computational domain extending 15 cylinder diameters away from the boundary, on a mesh with resolution 180x160. The predicted time history of the acoustic signal is further extracted from the unsteady flowfield solution and compared to the acoustic predictions based on the Potential-Theoretical Method[12], with the latter employing the near-field unsteady pressure results as an input. The acoustic directivities are compared at several radii to examine the accuracy of the direct numerical predictions.

In the following discussion, the governing equations, numerical method, and its implementation are first discussed, followed by a short overview of the acoustic prediction method and comparison of the numerical results.

----

[*] Visiting Assistant Professor, Member AIAA.

[†] Assistant Professor, Member AIAA.

[‡] Graduate Student Assistant, Member AIAA.

1

GOVERNING EQUATIONS

The unsteady Navier-Stokes equations, representing a system of conservation equations for mass, momentum, and energy in a viscous flow, can be written in vector notation as the sum of a volume and surface integral,

$$\frac{\partial}{\partial t} \int_{CV} \bar{Q}\, dV \;+\; \oint_{CS} \bar{F}\, dA \;=\; 0$$

where, for two-dimensional problems,

$$\bar{Q} = \begin{bmatrix} \rho \\ \rho u \\ \rho v \\ \rho e_o \end{bmatrix}, \qquad \bar{F} = \begin{bmatrix} \rho v_n \\ \rho u v_n - f_x \\ \rho v v_n - f_y \\ \rho h_o v_n - e_n \end{bmatrix}$$

and,

$$v_n = \vec{v} \cdot \hat{n} = u\,n_x + v\,n_y$$

$$n_x^2 + n_y^2 = 1$$

The stagnation energy and enthalpy per unit mass are defined as the sum of static and dynamic parts, respectively,

$$e_o = e + e_k , \qquad h_o = h + e_k$$

$$e_k = \tfrac{1}{2}\left(u^2 + v^2 \right)$$

with e_k being the kinetic energy per unit mass. Static energy, enthalpy, and pressure can all be expressed in terms of the local speed of sound a, a function of temperature, and the ratio of specific heats γ,

$$e = \frac{a^2}{\gamma(\gamma-1)} , \qquad h = \frac{a^2}{\gamma-1} , \qquad p = \frac{\rho\, a^2}{\gamma}$$

where,

$$a^2 = \gamma R T , \qquad \gamma = c_p / c_v$$

The energy flux e_n across a cell boundary, which is due to heat exchange as well the work done by the viscous stress tensor, is defined as follows,

$$e_n = \left(\vec{\bar{\tau}} \cdot \vec{v} - \vec{q} \right) \cdot \hat{n}$$

where,

$$\vec{\bar{\tau}} = \begin{bmatrix} \tau_{xx} & \tau_{xy} \\ \tau_{yx} & \tau_{yy} \end{bmatrix}, \qquad \vec{q} = \begin{pmatrix} q_x \\ q_y \end{pmatrix}$$

The force vector $\vec{f}$, which appears in the momentum equation, is the dot product of the stress tensor $\vec{\bar{\sigma}}$ and the outward unit normal to the local cell surface,

$$\vec{f} = \vec{\bar{\sigma}} \cdot \hat{n} = \begin{pmatrix} f_x \\ f_y \end{pmatrix}$$

where,

$$\vec{\bar{\sigma}} = \begin{bmatrix} \tau_{xx} - p & \tau_{xy} \\ \tau_{yx} & \tau_{yy} - p \end{bmatrix}$$

The components of the viscous stress tensor $\vec{\bar{\tau}}$, based on a Cartesian frame of reference, are determined through local velocity gradients,

$$\tau_{xx} = \frac{2}{3}\mu\left(2\frac{\partial u}{\partial x} - \frac{\partial v}{\partial y} \right)$$

$$\tau_{xy} = \mu\left(\frac{\partial v}{\partial x} + \frac{\partial u}{\partial y} \right) = \tau_{yx}$$

$$\tau_{yy} = \frac{2}{3}\mu\left(2\frac{\partial v}{\partial y} - \frac{\partial u}{\partial x} \right)$$

Similarly, the components of the heat flux vector $\vec{q}$ are determined through local temperature gradients according to Fourier's law of heat conduction,

$$q_x = -\kappa\frac{\partial T}{\partial x} , \qquad q_y = -\kappa\frac{\partial T}{\partial y}$$

NUMERICAL METHOD

In the applied numerical formulation, the Navier-Stokes equations are discretized and solved in time using first-order accurate explicit time marching. At each time level, the physical fluxes ($\bar{F}$) are summed over all four faces of the 2-D finite volume elements. A set of corrective eigenfluxes ($\vec{f}$), closely tied to the eigensystem of the inviscid Euler equations, is further added to the discretized equations in order to assure stability of the numerical scheme. Note that their presence renders the overall discretization total variation diminishing (TVD).

Denoting the spatial locations with subscript indices and time levels with superscript indices, the discretized equations become,

$$\bar{Q}_{i,j}^{p+1} = \bar{Q}_{i,j}^{p} - \frac{\Delta t}{\Delta V_{i,j}}\Big\{\big(\bar{F}_{i+1/2,j}\,\Delta A_{i+1/2,j} + \bar{F}_{i,j+1/2}\,\Delta A_{i,j+1/2}\big)$$

$$- \big(\bar{F}_{i-1/2,j}\,\Delta A_{i-1/2,j} + \bar{F}_{i,j-1/2}\,\Delta A_{i,j-1/2}\big)\Big\}$$

$$+ \frac{1}{2}\Big\{\big(\bar{f}_{i+1/2,j} + \bar{f}_{i,j+1/2}\big) - \big(\bar{f}_{i-1/2,j} + \bar{f}_{i,j-1/2}\big)\Big\}$$

where,

$$\bar{F}_{i+1/2,j} = \tfrac{1}{2}\bar{F}(\bar{Q}_{i,j}^{p}) + \tfrac{1}{2}\bar{F}(\bar{Q}_{i+1,j}^{p})$$

$$\bar{F}_{i-1/2,j} = \tfrac{1}{2}\bar{F}(\bar{Q}_{i,j}^{p}) + \tfrac{1}{2}\bar{F}(\bar{Q}_{i-1,j}^{p})$$

The eigenfluxes are constructed according to Harten's[1] original TVD scheme, with one significant modification: instead of using the numerical viscosity function of the form,

$$\text{Viscos}(x) = \begin{cases} \tfrac{1}{2}\big(x^2/\varepsilon + \varepsilon\big) & \text{if } |x| \le \varepsilon \\ |x| & \text{if } |x| > \varepsilon \end{cases}$$

$$0 < \varepsilon \le 0.5$$

the absolute value function, $\text{Abs}(x) = |x|$, was used in all successive formulas. Such practice is equivalent to setting the numerical viscosity parameter $\varepsilon = 0$. Thus, we obtain,

$$\bar{f}_{i+1/2,j} = \bar{\bar{R}}_{i+1/2,j} \cdot \bar{b}_{i+1/2,j}$$

$$\bar{\bar{R}}_{i+1/2,j} = \bar{\bar{R}}(\bar{Q}_{i+1/2,j}^{p}), \quad \bar{Q}_{i+1/2,j}^{p} = \frac{1}{2}\big(\bar{Q}_{i,j}^{p} + \bar{Q}_{i+1,j}^{p}\big)$$

$$\bar{b}_{i+1/2,j} = \text{Abs}\big(\bar{l}_{i+1/2,j} + \bar{m}_{i+1/2,j}\big)\,\bar{a}_{i+1/2,j} - \big(\bar{u}_{i,j} + \bar{u}_{i+1,j}\big)$$

$$\bar{a}_{i+1/2,j} = \bar{\bar{L}}_{i+1/2,j} \cdot \Delta\bar{Q}_{i+1/2,j}^{p}$$

$$\Delta\bar{Q}_{i+1/2,j}^{p} = \bar{Q}_{i+1,j}^{p} - \bar{Q}_{i,j}^{p}, \quad \bar{\bar{L}}_{i+1/2,j} = \bar{\bar{L}}(\bar{Q}_{i+1/2,j}^{p})$$

where $\bar{\bar{R}}$ and $\bar{\bar{L}}$ are the matrices of the right and left eigenvectors of the Euler equations in the normal vector format,

$$\bar{\bar{R}} = \begin{bmatrix} 1 & 1 & 1 & 0 \\ u - a\,n_x & u & u + a\,n_x & n_y \\ v - a\,n_y & v & v + a\,n_y & -n_x \\ h_o - a\,v_n & e_k & h_o + a\,v_n & u\,n_y - v\,n_x \end{bmatrix}$$

$$\bar{\bar{L}} = \begin{bmatrix} \dfrac{(\gamma-1)\,e_k + a\,v_n}{2\,a^2} & \dfrac{(1-\gamma)\,u - a\,n_x}{2\,a^2} & \dfrac{(1-\gamma)\,v - a\,n_y}{2\,a^2} & \dfrac{\gamma-1}{2\,a^2} \\[2mm] \dfrac{a^2 - (\gamma-1)\,e_k}{a^2} & \dfrac{(\gamma-1)\,u}{a^2} & \dfrac{(\gamma-1)\,v}{a^2} & \dfrac{1-\gamma}{a^2} \\[2mm] \dfrac{(\gamma-1)\,e_k - a\,v_n}{2\,a^2} & \dfrac{(1-\gamma)\,u + a\,n_x}{2\,a^2} & \dfrac{(1-\gamma)\,v + a\,n_y}{2\,a^2} & \dfrac{\gamma-1}{2\,a^2} \\[2mm] v\,n_x - u\,n_y & n_y & -n_x & 0 \end{bmatrix}$$

The flux correction terms $\bar{u}$ and $\bar{m}$ are calculated based on the Minmod flux limiter function,

$$\bar{m}_{i+1/2,j} = \big(\bar{u}_{i+1,j} - \bar{u}_{i,j}\big)\big/\bar{a}_{i+1/2,j} \quad \text{if } \bar{a}_{i+1/2,j} \ne 0$$

$$= 0 \quad\quad\quad\quad\quad\quad\quad \text{if } \bar{a}_{i+1/2,j} = 0$$

$$\bar{u}_{i,j} = \bar{\mathcal{S}}_{\bar{w}}\,\text{Minmod}\big(\big|\bar{w}_{i+1/2,j}\big|, \bar{w}_{i-1/2,j}\,\bar{\mathcal{S}}_{\bar{w}}\big)$$

$$\bar{\mathcal{S}}_{\bar{w}} = \text{sgn}(\bar{w}_{i+1/2,j})$$

$$\bar{w}_{i+1/2,j} = \tfrac{1}{2}\big(\text{Abs}(\bar{l}_{i+1/2,j}) - (\bar{l}_{i+1/2,j})^2\big)\,\bar{a}_{i+1/2,j}$$

where $\text{Minmod}(x,y) = \max\big[0, \min(x,y)\big]$.

The eigenvalues $\bar{\lambda}$ are non-dimensionalized by τ, the ratio of integration time step and local cell spacing,

$$\bar{l}_{i+1/2,j} = \bar{\lambda}_{i+1/2,j}\,\tau_{i+1/2,j}$$

$$\tau_{i+1/2,j} = \frac{\Delta t\,\Delta A_{i+1/2,j}}{\tfrac{1}{2}\big(\Delta V_{i,j} + \Delta V_{i+1,j}\big)}$$

$$\bar{\lambda}_{i+1/2,j} = \bar{\lambda}(\bar{Q}_{i+1/2,j}^{p}) = \begin{bmatrix} v_n - a \\ v_n \\ v_n + a \\ v_n \end{bmatrix}_{i+1/2,j}$$

In all calculations, the flowfield is initialized impulsively, i.e., all the fluid cells in the interior computational domain are assigned the free stream values. Afterwards, the far-field boundary cells are

3

maintained at the free stream conditions. A no-slip condition is implemented at the solid boundary together with a pressure-density gradient extrapolation based on the adiabatic wall condition.

COMPUTATIONAL RESULTS

After the mean flow has traveled approximately 100 cylinder diameters from its impulsive beginning, the alternate vortex shedding initiated, and a von Karman vortex street develops in the wake. Figure 1 shows two Mach number plots taken 10ms after the impulsive start, at which point periodicity of the shedding process fully sets in. The upper plot shows the propagation of the wake towards the far-field boundary. The lower picture, enlarged by a factor of ten, reveals a small region of locally supersonic flow followed by a transonic shock impinging on the cylinder's surface, with subsequent boundary layer separation. The lift, drag, and moment coefficients were recorded between 10ms and 20ms of simulation time. Figure 2 shows the time history of the aerodynamic coefficients that clearly demonstrates periodicity of the flow, and also indicates the presence of additional high and low frequency content, characteristic of this Reynolds number regime[11].

Figure 1b: Mach number contours at 10ms (enlarged view)
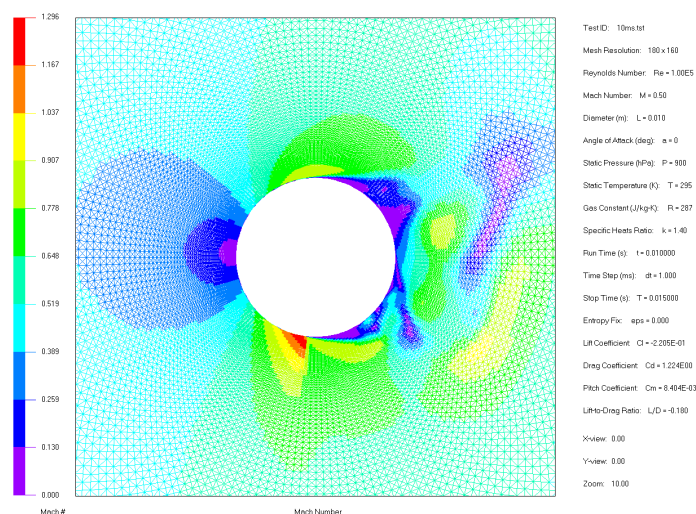

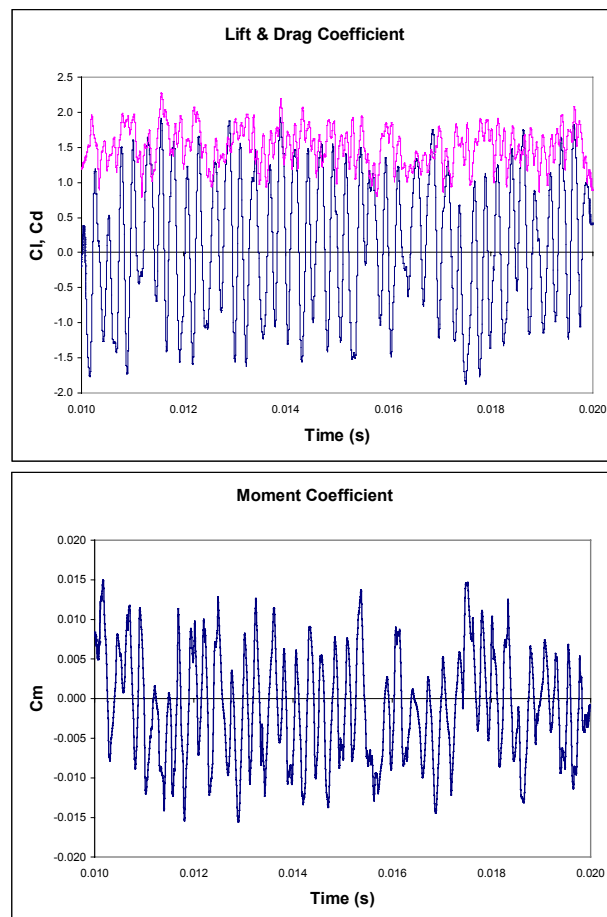Figure 1a: View of the computational domain with Mach number contours at 10ms

Figure 2: Aerodynamic coefficients versus time

4

ACOUSTIC ANALYSIS OF NUMERICAL DATA

To extract the acoustic signal contained in the unsteady numerical solution, the time history of the unsteady pressure was recorded at several radii corresponding to $r/D = 1, 5, 10$, as well as on the surface of the cylinder, $r/D = 0.5$. The data was later processed through a Fast Fourier Transform in order to examine its frequency content and dominant harmonics. Some of the results from this analysis are illustrated in Figures 3-8.

In Figure 3, a typical time history of the unsteady pressure solution is shown as recorded at the radial locations corresponding to $r/D = 0.5, 1, 5,$ and 10, at the same angular position of 90 deg. (above the cylinder). Once the mean flow has converged, the time history is calculated for a period of 3ms by marching through 14,754 steps with a time step of approximately $2*10^{-7}$ s. This provided for a minimum frequency resolution corresponding to a Strouhal number $St = f D/U = 0.02$, where $f = \omega/2\pi$ is the frequency in Hertz. Figure 4 shows the FFT-produced frequency spectrum of the unsteady pressure signals calculated by the code at the angular locations $\theta = 0, 90, 180$ and 270 deg. on the surface of the cylinder ($r/D = 0.5$). Note that results for 90 and 270 deg. (the upper and bottom points) are expected to be almost identical due to the upstream flow symmetry. As can be seen from the plot, the pressure fluctuations on the surface of the cylinder appear highest at those two points, with the dominant frequency corresponding to $St = 0.23$, which is very close to the expected Aeolian tone frequency.

The results in Figures 5-7 are shown for the same angular locations, for the radii $r/D = 1, 5,$ and 10, correspondingly. While the same maximum of the spectral energy persists at the locations above and below the cylinder, the total unsteady pressure response appears dominated by pressure fluctuations in the wake region ($\theta = 0$ deg.) with a broad frequency content. Interestingly enough, as the flow moves further downstream, the maximum of pulsations is recorded at $r/D = 5$, which points the presence of a shed vortex at this location (compared to $r/D = 1$). Furthermore, downstream at $r/D = 1$, the dominant frequency is close to the acoustic one, and the same frequency dominates in the far field ($r/D = 10$) where the aerodynamic wake pulsations have already significantly reduced (this correspondence is also seen from the flowfield pattern in Figure 1). Note, however, that the

dominant frequency appears shifted to the left relative to $St = 0.23$ observed elsewhere.
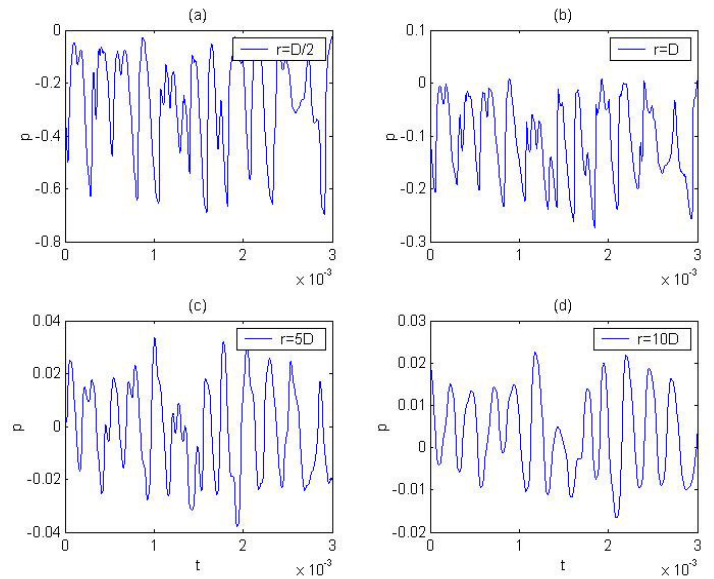

Figure 3: Recorded time history (3ms) of unsteady pressure at $\theta = 90$ deg., $r = 0.5D, D, 5D,$ and $10D$
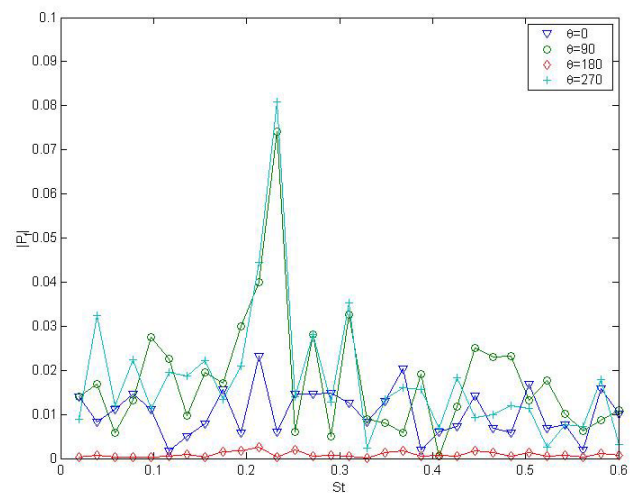

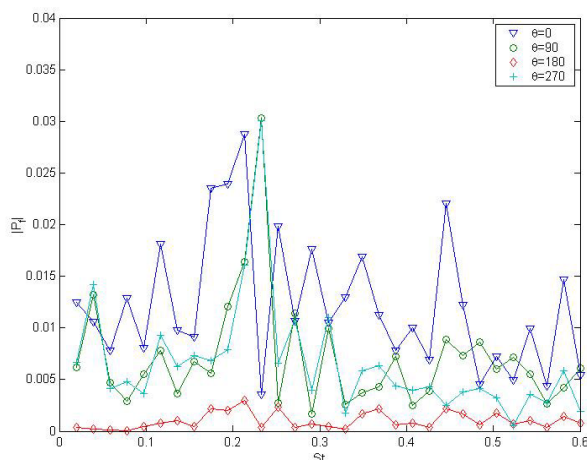Figure 4: FFT of unsteady pressure at $\theta = 0, 90, 180$ and 270 deg., $r = 0.5D$ (surface of the cylinder)

5

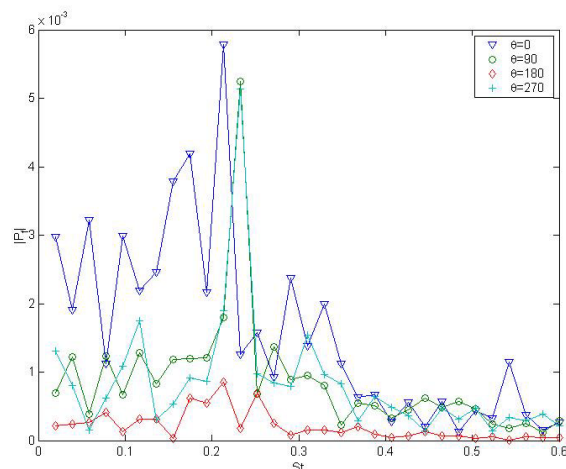Figure 5: FFT of unsteady pressure at $\theta = 0$, 90, 180 and 270 deg., $r = D$

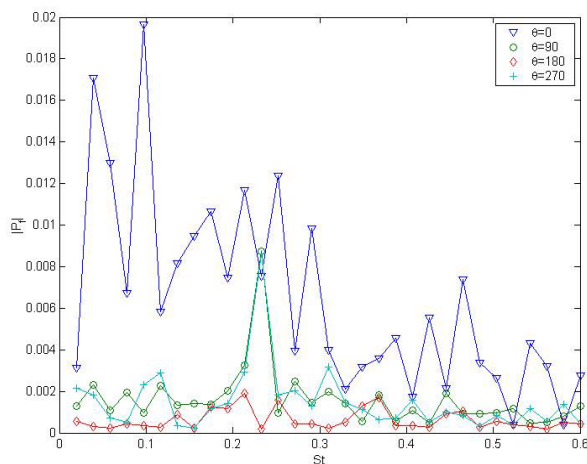Figure 7: FFT of unsteady pressure at $\theta = 0$, 90, 180 and 270 deg., $r = 10D$

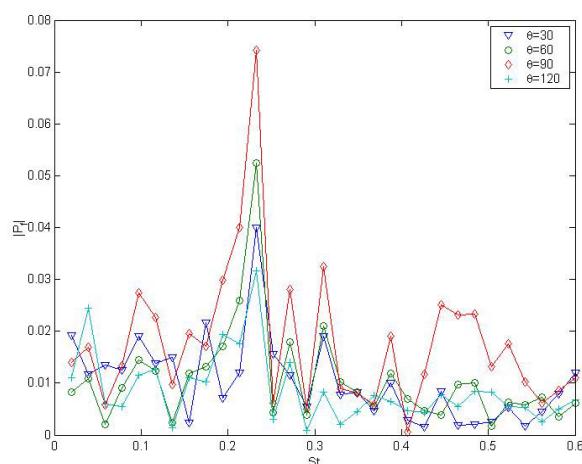Figure 6: FFT of unsteady pressure at $\theta = 0$, 90, 180 and 270 deg., $r = 5D$

Figure 8: FFT of unsteady pressure at $\theta = 30$, 60, 90 and 120 deg., $r = 10D$

Finally, Figure 8 presents a more detailed analysis of the obtained far-field frequency spectrum at 4 angular locations in the upper half of the plane, corresponding to $\theta = 30$, 60, 90 and 120 deg. The position above the cylinder shows the maximum acoustic power at $St = 0.23$, which corresponds to the dipole-type acoustic radiation due to the oscillating unsteady forces on the cylinder. This feature is clearly observed in Figure 9, showing a directivity plot for the unsteady pressure harmonic corresponding to $St = 0.23$. The acoustic directivity results will be compared to the acoustic predictions based on the Potential-Theoretical Method, which is first briefly described.

POTENTIAL-THEORETICAL METHOD

The Potential-Theoretical Method recently developed in Ref. 12 belongs to a family of Kirchhoff-surface techniques relying on the near-field flow data to propagate acoustic information to the far-field through the linear flow region. The Kirchhoff control surface should encompass the flow region containing all the acoustic sources. With the assumption that the acoustic propagation outside of the control surface is governed by a simple wave equation, the acoustic solution in the far-field can be obtained in terms of an integral over the Kirchhoff surface, involving some form of the Green function convoluted with the near-field acoustic source information on the control surface. Different formulations involve various

6

techniques to represent the required Green function and select the type of the near-field flow information on the control surface. In the classical Kirchhoff approach[13], the free-space Green function is used along with the acoustic source's unsteady pressure and its time and normal derivatives. Other approaches[14-15] have used the method of images to construct a special form of the Green function to eliminate the need to estimate source pressure derivatives on the control surface. The current approach achieves the same task of employing only the unsteady pressure information on the control surface, but at the same time it requires only a free-stream Green function, thus making the method particularly flexible to any shape of the control surface. For instance, the latter can coincide with the mesh used in a flow simulation, thus avoiding any interpolation errors.

As any Kirchhoff-type approach, the method is implemented with the assumption that the acoustic frequency harmonics radiating from the control surface are governed by the Helmholtz equation,

$$\tilde{\nabla}^2 P_f + K^2 P_f = 0$$

where P_f is the particular frequency harmonic of the pressure, and tilde implies that a transformation to the Prandtl-Glauert plane may be required for simulations performed with a uniform flow. For the current problem of the flow around a cylinder, the computations are performed in the physical plane. Thus, the Helmholtz equation applies as is, with the Helmholtz number $K = \omega / c_S = 2\pi \, St \, M$, where c_S is the speed of sound.
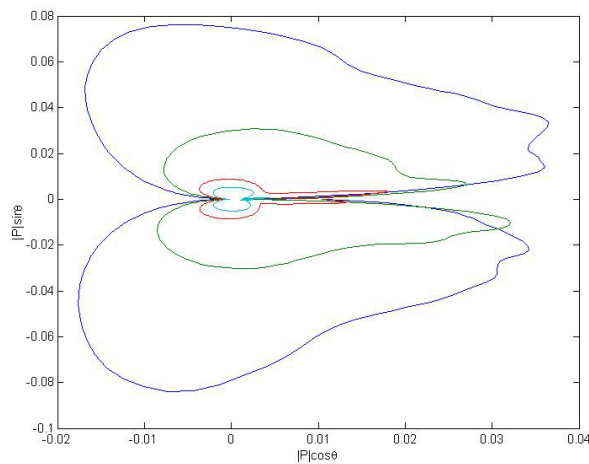
Figure 9. Directivity of the unsteady pressure harmonic corresponding to the acoustic frequency of *St*=0.23. *r/D*=0.5, 1, 5, 10 (with amplitude decreasing in this order).
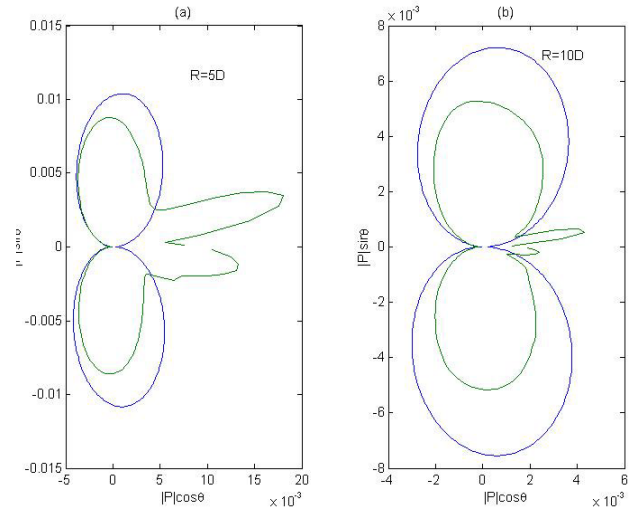
Figure 10: Comparison of the computed acoustic directivity with PTM predictions based on the near-field pressure from the surface of the cylinder (*r/D*=0.5). Results for *St*=0.23, (a) *r/D*=5 (b) *r/D*=10 (direct simulations show wake effect).
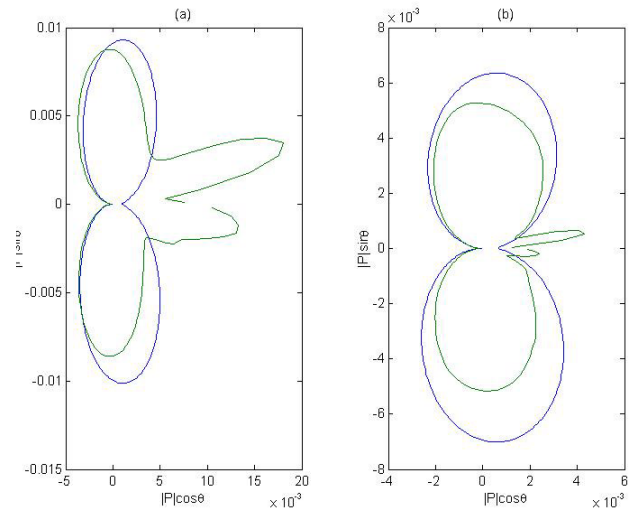
Figure 11: Comparison of the computed acoustic directivity with PTM predictions based on the near-field pressure from the control surface at *r/D*=1. Results for *St*=0.23, (a) *r/D*=5, (b) *r/D*=10 (direct simulations show wake effect).

COMPARISON OF ACOUSTIC PREDICTIONS

Finally, in this Section, we compare results obtained for the acoustic directivity of the $St = 0.23$ harmonic, both based on the code simulations and the Potential-Theoretical Method. These results are presented in Figures 10 and 11 for far-field circles located at $r/D = 5$ (a) and $r/D = 10$ (b). In Figure 10, the near-field unsteady pressure from the CFD code is supplied to the PTM code at the control surface

7

coincident with the surface of the cylinder, thus taking into account only the effect from the unsteady forces on the cylinder. In Figure 11, the near-field pressure is taken on the circle $r/D = 1$. One may note that no acoustic sources radiating at the frequency of $St = 0.23$ are expected beyond the surface of the cylinder, thus the results should remain practically the same.

Overall, the comparison indicates that while the employed low-order modified TVD scheme still exhibits the numerical dissipation characteristic of such types of schemes, the level of dissipation appears rather moderate as the numerical solution maintains the dominant directivity shape. The computed amplitude appears slowly deteriorating relative to the PTM predictions as the far-field circle is transferred further from $r/D = 5$ to 10. Note that the results in Figure 11 actually appear closer compared to those in Figure 10, but this can be explained by the fact that the near-field pressure data taken on the control surface at $r/D = 1$ contains already a slightly dissipated solution. This is also confirmed in Figure 12 comparing the acoustic directivities obtained using the PTM code with the two control surface locations.
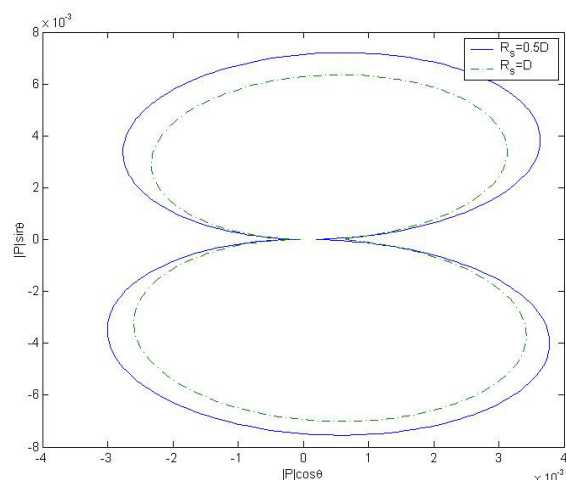

Figure 12: Acoustic directivities from the PTM predictions based on near-field pressure from two control surface locations: at r/D=0.5 (solid line) and at r/D=1 (dashed line). Results for St=0.23, r/D=10.

CONCLUSIONS

The present work introduced a new CAA code based on a low-order modified TVD scheme for unsteady, compressible, viscous flow simulations. To validate the accuracy of the code, a test benchmark case was run for the viscous 2-D flow over a cylinder at a Mach number of 0.5 and a diameter-based Reynolds number of 100,000. The results for the directly resolved acoustic signature in the far-field were compared with the acoustic predictions based on the Potential-Theoretical Method that used the near-field unsteady pressure information from the CFD code (on a selected control surface) as an input. The comparison of the acoustic directivities revealed that while numerical dissipation remained present in the direct numerical simulation, the level of dissipation appeared rather moderate, and both the characteristic radiation frequency and the dipole-type directivity produced by the wake-induced unsteady forces on the surface of the cylinder were well resolved.

REFERENCES

[1] Harten, Ami. *High Resolution Schemes for Hyperbolic Conservation Laws.* Journal of Computational Physics, Volume 49, 1983, pp. 357-393.

[2] Yee, H.C., R.F. Warming, and Ami Harten. *"On a Class of TVD Schemes for Gas Dynamic Calculations", Numerical Methods of the Euler Equations of Fluid Dynamics.* Edited by F. Angrand, A. Dervieux, J.A. Desideri, and R. Glowinski. Society for Industrial and Applied Mathematics, Philadelphia, PA, 1985, pp. 84-107.

[3] Wang, Z., and B.E. Richards. *High Resolution Schemes for Steady Flow Computation.* Journal of Computational Physics, Volume 97, 1991, pp. 53-72.

[4] Smithwick, Quinn, and Scott Eberhardt. *Fuzzy Controller and Neuron Models of Harten's Second-Order TVD Scheme.* AIAA Journal, Volume 32, No. 10, 1994, pp. 2122-2124.

[5] Jeng, Yih Nen, and Uon Jan Payne. *An Adaptive TVD Limiter.* Journal of Computational Physics, Volume 118, 1995, pp. 229-241.

[6] Yee, H.C., and P. Kutler. *Application of Second-Order-Accurate TVD Schemes to the Euler Equations in General Geometries.* NASA Technical Memorandum, TM 85845, 1983.

[7] Wang, J.C.T., and G.F. Widhopf. *A High-Resolution TVD Finite Volume Scheme for the Euler Equations in Conservation Form.* Journal of Computational Physics, Volume 84, 1989, pp. 145-173.

[8] Lu, Pong-Jeu, and Kuen-Chuan Wu. *Assessment of TVD Schemes in Compressible Mixing Flow Computations.* AIAA Journal, Volume 30, No. 4, 1992, pp. 939-946.

[9] Li, X.L., B.X. Jin, and J. Glimm. *Numerical Study for the Three-Dimensional Rayleigh-Taylor Instability through the TVD/AC Scheme and Parallel Computation.* Journal of Computational Physics, Volume 126, 1996, pp. 343-355.

[10] Rohde, Axel. *A Computational Study of Flow Around a Rotating Disc in Flight.* Dissertation in Aerospace Engineering, Florida Institute of Technology, 2000. Published via the author's website, www.microcfd.com.

[11] Kenneth, B.S., Rumsey, C.L., Cox, J.S., and B.A. Younis. *"Computation of Sound Generated by Flow over a Circular Cylinder: An Acoustic Analogy Approach", Second Computational Aeroacoustics Workshop on Benchmark Problems.* Edited by C.K.W. Tam and J.C. Hardin, NASA CP 3352, 1996.

[12] Hariharan, S.I., Scott, J.R., and K.L. Kreider. *A Potential-Theoretical Method for Far-Field Sound Radiation Calculations.* Journal of Computational Physics, Volume 164, 2000, pp. 143-164.

[13] Lyrintzis, A.S. *The Use of Kirchhoff's Method in Computational Aeroacoustics.* ASME Journal of Fluids Engineering, Volume 116, 1994, pp. 665-676.

[14] Atassi, H.M, Dusey, M., and C.M. Davis. *Acoustic Radiation from a Thin Airfoil in Nonuniform Subsonic Flow.* AIAA Journal, Volume 31, 1993, pp. 12-19.

[15] Mankbadi, R.R., Shih, S.-H., Hixon, D.R., Stuart, J.T., and L.A. Povinelli. *A Surface-Integral Formulation for Jet Noise Prediction Based on the Pressure Signal Alone.* Journal of Computational Acoustics, Volume 6, 1998, pp. 307-320.